



Cite this: *Phys. Chem. Chem. Phys.*,
2019, 21, 4779

Oxygen surface exchange and diffusion in $\text{Pr}_{1.75}\text{Sr}_{0.25}\text{Ni}_{0.75}\text{Co}_{0.25}\text{O}_{4\pm\delta}$

Evgeniy Tropin,^{id ab} Maxim Ananyev,^{id ab} Natalia Porotnikova,^{id *ab}
Anna Khodimchuk,^{id ab} Saim Saher,^{id c} Andrey Farlenkov,^{id ab}
Edhem Kurumchin,^{id a} Denis Shepel,^d Evgeny Antipov,^{id e} Sergei Istomin^{id ef} and
Henny Bouwmeester^{id c}

Oxygen surface exchange and diffusion in $\text{Pr}_{1.75}\text{Sr}_{0.25}\text{Ni}_{0.75}\text{Co}_{0.25}\text{O}_{4\pm\delta}$ have been investigated using two methods: pulsed isotope exchange (PIE) and oxygen isotope exchange with gas phase equilibration (IE GPE). Oxygen surface exchange kinetics is considered in the framework of two-step models including two consecutive stages: dissociative adsorption of oxygen and incorporation of oxygen adatoms into the crystal lattice. The rates of oxygen heterogeneous exchange (r_{H}) as well as the rates of dissociative adsorption (r_{a}) and oxygen incorporation (r_{i}) have been calculated. The applicability of the two-step model is discussed based on the concept of a novel two-step mechanism with distributed rates of dissociative adsorption and incorporation of oxygen. It is shown that the two-step model can be applicable for the description of oxygen exchange kinetics in $\text{Pr}_{1.75}\text{Sr}_{0.25}\text{Ni}_{0.75}\text{Co}_{0.25}\text{O}_{4\pm\delta}$ only at temperatures below 750 °C. Above this temperature, only the statistical model with distributed rates can be used. At low temperatures (<750 °C), the oxygen incorporation rate is found to be smaller than the rate of oxygen dissociative adsorption. Thus, under these experimental conditions the stage of oxygen incorporation is considered to be rate-determining. When increasing the temperature, the difference between r_{a} and r_{i} decreases and the stages become competing. The oxygen isotope exchange kinetic profiles obtained using the IE GPE method are found to be complicated and include a surface exchange stage as well as at least two diffusion relaxation processes. The reasons for the existence of these two processes are discussed.

Received 10th January 2019,
Accepted 6th February 2019

DOI: 10.1039/c9cp00172g

rsc.li/pccp

1. Introduction

In the face of continuous environmental degradation, one of the major challenges is the reduction of harmful emissions and lowering the dependence on hydrocarbon fuels. The attractiveness of using solid oxide fuel cells (SOFCs) in the furtherance of this goal is primarily due to the high efficiency of the direct conversion of the chemical energy of fuels to electricity and nonpolluting reaction products. The creation of stable oxygen electrodes for medium-temperature fuel cells is a priority area of research in the field of SOFCs.

Complex oxides of the general formula $\text{Ln}_2\text{NiO}_{4+\delta}$ (Ln-rare earth elements, such as La, Pr, and Nd) with the $n = 1$

Ruddlesden–Popper $\text{A}_{n+1}\text{B}_n\text{O}_{3n+1}$ type structure are promising for use as materials for electrochemical devices, *e.g.* gas sensors, oxygen permeation mixed ionic–electronic membranes, solid oxide electrolyser cells (SOECs) and solid oxide fuel cells.^{1–7} The crystal structure of nickelates belonging to the Ruddlesden–Popper series can be described as an intergrowth of LnNiO_3 perovskite slabs separated by LnO rock-salt slabs.⁸ Hyperstoichiometric (δ) oxygen atoms localize in the empty tetrahedra of LnO rock-salt slabs, reducing the strain between Ln–O and Ni–O bonds. The alternating perovskite and rock salt layers in the $n = 1$ Ruddlesden–Popper structure can be a reason for different oxygen diffusion and surface exchange kinetics along different crystallographic directions.⁹ These oxides possess high electron and oxygen ionic conductivity along with high catalytic activity with respect to the oxygen reduction reaction in the oxidizing atmosphere.^{10–12} The processes of oxygen exchange between the oxide and the gas phase have a determining effect on the operation of electrodes of the electrochemical devices.

Among rare earth metal nickelates, those with Pr possess the highest oxygen ion conductivity¹³ together with the smallest

^a Institute of High Temperature Electrochemistry, Ekaterinburg 620137, Russia.
E-mail: n.porotnikova@mail.ru

^b Ural Federal University, Ekaterinburg 620002, Russia

^c University of Twente, Science and Technology, 7500 AE Enschede, The Netherlands

^d Technoinfo Ltd, Moscow 121248, Russia

^e Lomonosov Moscow State University, Moscow 119991, Russia

^f National Research University Higher School of Economics, 20 Myasnitskaya str., Moscow, 101000, Russia

polarization¹⁴ and area-specific resistance.¹⁵ However, few works dedicated to pure $\text{Pr}_2\text{NiO}_{4+\delta}$ as SOFC cathodes are found in the literature. This may be due to the generally accepted thermodynamic metastability of the $\text{Pr}_2\text{NiO}_{4+\delta}$ phase at temperatures in the range of 800–950 °C in oxidizing atmospheres. It was found that, at these temperatures, $\text{Pr}_2\text{NiO}_{4+\delta}$ decomposes into higher order Ruddlesden–Popper phases and praseodymium oxide-based phases.^{16–18} Stabilization of the structure, increasing the electron conductivity and thermal stability, can be achieved by cation substitution in A and B-sublattices.

According to previous reports, A-site doping by alkaline-earth metals (e.g., Sr, Ca, and Ba) provides an effective route to further increase the electrical conductivity by the formation of electron holes, oxygen vacancies or oxygen interstitials. Solid solution $\text{Pr}_{2-x}\text{Sr}_x\text{NiO}_{4+\delta}$ where $x = 0.5, 0.7, 0.9$ and 1.0 was investigated in ref. 19. The maximal electrical conductivity was found to be 0.39 S cm^{-1} at 700 °C in $\text{Pr}_{1.3}\text{Sr}_{0.7}\text{NiO}_{4+\delta}$. The minimal area-specific resistance (ASR) of $0.39 \text{ } \Omega \text{ cm}^2$ at 700 °C is obtained at $x = 0.7$ and is attributed to the highest electrical conductivity in a row.¹⁹ The increase in the Sr content is accompanied by a decrease in the hyperstoichiometric oxygen content, leading to oxygen-deficient phases. The values of x at which δ is negative are not well defined and vary depending upon the synthesis conditions.^{20–22}

Partial substitution of Ni with other 3d-metals (e.g. Co) was found to increase ionic conductivity, which would enhance the performance of these substituted oxides as cathode materials. $\text{Pr}_{2-x}\text{Sr}_x\text{Ni}_{1-x}\text{Co}_x\text{O}_{4+\delta}$ ($x = 0.25, 0.5,$ and 0.75) oxides have recently been studied.²³ The studies on the thermal expansion coefficients, electrical conductivity in air, chemical stability in oxidizing atmospheres and compatibility with gadolinia-doped ceria at high temperatures reveal the optimal composition of $\text{Pr}_{1.35}\text{Sr}_{0.65}\text{Ni}_{0.75}\text{Co}_{0.25}\text{O}_{4+\delta}$. This compound is stable in oxygen at 900 °C and does not react with ceria-based electrolytes at least up to 1200 °C. It possesses a relatively low thermal expansion coefficient of 13 ppm K^{-1} and electrical conductivity in air of 280 S cm^{-1} at 900 °C, thus representing a promising composition for use as a cathode material in intermediate temperature solid oxide fuel cells (IT-SOFCs).²¹ Nevertheless, taking into account the easiness of Sr segregation at elevated temperatures in perovskites and Ruddlesden–Popper phases,^{24–26} we believe that a large strontium content can negatively affect the stability of the electrochemical performance of $\text{Pr}_{2-x}\text{Sr}_x\text{Ni}_{1-y}\text{Co}_y\text{O}_{4+\delta}$ based electrodes. In order to harmonize electrical properties and thermal stability, the composition of $\text{Pr}_{1.75}\text{Sr}_{0.25}\text{Ni}_{0.75}\text{Co}_{0.25}\text{O}_{4\pm\delta}$ was chosen for further investigation of oxygen surface exchange and diffusion.

In recent works^{13,27–32} the oxygen exchange kinetics was investigated in $\text{La}_2\text{NiO}_{4+\delta}$. The oxygen diffusion in $\text{La}_2\text{NiO}_{4+\delta}$ has been extensively studied using the isotope exchange depth-profiling method with secondary ion mass-spectrometry (IEDP-SIMS) on monocrystalline samples,¹³ polycrystalline ceramics²⁸ and thin film specimens.³¹ Strong anisotropy of diffusion was observed due to a layered structure of $\text{La}_2\text{NiO}_{4+\delta}$.^{13,30} The inhomogeneity of the $\text{La}_2\text{NiO}_{4+\delta}$ surface towards the oxygen exchange process was observed in ref. 9. The electron backscatter

diffraction analysis of the $\text{La}_2\text{NiO}_{4+\delta}$ surface revealed the presence of grains with different crystallographic orientations in the polycrystalline structure, such that the authors concluded that the abovementioned inhomogeneity can be associated with the existence of kinetically not equivalent apical and equatorial La–O sites.⁹ The alkaline-earth metal (Ca) doping led to the increase in electrical conductivity;³³ however, the oxygen surface exchange (k^*) and oxygen tracer diffusion (D^*) coefficients significantly decreased in comparison with undoped lanthanum nickelates.³⁴ The change of the rate-determining stage was also observed upon Ca doping. While for $\text{La}_2\text{NiO}_{4+\delta}$ this stage represented dissociative adsorption, for $\text{La}_{1.7}\text{Ca}_{0.3}\text{NiO}_{4\pm\delta}$ oxygen incorporation represented the rate-determining stage. Using the C^{18}O_2 SSITKA method,³³ the total oxygen mobility in the doped materials $\text{Ln}_{2-x}\text{Ca}_x\text{NiO}_{4+\delta}$ ($\text{Ln} = \text{La}, \text{Pr}, \text{Nd}; x = 0; 0.3$) was shown to fall with doping due to a decrease in the content of highly mobile interstitial oxygen and hampering of the cooperative oxygen transport mechanism.

In the case of $\text{Pr}_2\text{NiO}_{4+\delta}$, a nonlinear temperature dependence of the oxygen surface exchange rate was obtained in Arrhenius coordinates compared to $\text{La}_2\text{NiO}_{4+\delta}$.^{9,35} In these papers, it was shown that the change in the oxygen surface exchange power indices depending on temperature is associated with the change in the ratio between the oxygen dissociative adsorption and oxygen incorporation rates. The change in the rate-determining stage of the oxygen exchange occurs due to the segregation of PrO_x oxide.

In the present work, two methods were used to investigate oxygen surface exchange and diffusion in $\text{Pr}_{1.75}\text{Sr}_{0.25}\text{Ni}_{0.75}\text{Co}_{0.25}\text{O}_{4\pm\delta}$: the pulsed isotope exchange (PIE) and the isotope exchange with gas phase equilibration (IE GPE). Pulsed isotope exchange is an express technique that allows the use of relatively high oxygen partial pressure (10^{-2} –1.0 atm). However, this method does not provide information on oxygen diffusion. Isotope exchange with gas phase equilibration gives full kinetic information, including oxygen surface exchange (k) and oxygen diffusion coefficient (D) values. One of the major drawbacks of this method, however, is the very narrow oxygen partial pressure range (10^{-3} – 10^{-1} atm), due to the necessity of maintaining the number of tracer molecules in the gas phase (N_g) considerably less than the number of tracer molecules in solid oxide (N_o). In order to obtain comprehensive information about the oxygen surface exchange and diffusion in the wide range of experimental conditions (oxygen partial pressure and temperature), both methods were used and good agreement is observed between the sets of data. It is worth mentioning that PIE data can only be processed assuming the so-called two-step model of oxygen exchange (which is discussed further), while IE GPE data allow the verification of a model of oxygen exchange in every particular case (for every particular sample and experimental conditions). Such verification is made in the present work for $\text{Pr}_{1.75}\text{Sr}_{0.25}\text{Ni}_{0.75}\text{Co}_{0.25}\text{O}_{4\pm\delta}$ samples.

2. Experimental

The $\text{Pr}_{1.75}\text{Sr}_{0.25}\text{Ni}_{0.75}\text{Co}_{0.25}\text{O}_{4\pm\delta}$ samples were prepared using the citrate-nitrate method. Starting reagents Pr_6O_{11} , SrCO_3 ,

NiO, and $\text{Co}(\text{NO}_3)_2 \cdot \text{H}_2\text{O}$ of high purity grade were dissolved in nitric acid and mixed in the stoichiometric ratio. After that, citric acid was added and the solution was evaporated at 200 °C, followed by firing at 950 °C for 2 h. The final annealing was performed at 1200 °C for 3 h. After that, the powder was ground, pressed into pellets and sintered at 1450 °C for 5 h to obtain dense ceramic samples (98%) for the isotope exchange with gas phase equilibration (IE GPE) experiment. Dense ceramics were polished with successive grades of diamond paste (ASM 7/5 NVM, grit size 5–7 μm and ASM 1/0 NOM, grit size 1 μm). A powder of $\text{Pr}_{1.75}\text{Sr}_{0.25}\text{Ni}_{0.75}\text{Co}_{0.25}\text{O}_{4\pm\delta}$ was used for the pulsed isotope exchange (PIE) method. Experiments using both methods (PIE and IE GPE) were carried out on samples from one batch of the synthesis.

Particle size analysis of the powder was carried out on the laser diffraction analyzer Malvern Mastersizer 2000. The average particle size was about 15 μm . The specific surface area determined using the BET (Brunauer–Emmett–Teller) method on a SORBI N4.1 instrument was $1.58 \pm 0.07 \text{ m}^2 \text{ g}^{-1}$. This value was used for the oxygen exchange rate calculation in the case of the PIE.

The chemical composition of the samples was controlled *via* atomic emission spectroscopy employing the inductively coupled plasma (ICP–AES) technique using a PerkinElmer Optima 4300 DV spectrometer. The cation compositions of the powdered ceramic samples are stoichiometric and listed in Table 1.

The X-ray diffraction (XRD) study was carried out on a Rigaku D/MAX-2200VL/PC diffractometer using Cu K α radiation ($\lambda = 1.5418 \text{ \AA}$) in the range of $10^\circ < 2\theta < 100^\circ$ (Fig. 1a). XRD analysis showed the presence of nickel oxide and praseodymium oxide based admixture phases. Reflections from NiO and Pr_2O_3 oxides were observed in XRD patterns, as shown in Fig. 1b. The refined weight fractions of NiO and Pr_2O_3 in the sample were 1 wt% and 0.5 wt%, respectively. However, their refined content was too small to have a significant influence on the oxygen isotope kinetic study.

Microstructure characterization and elemental analysis of the $\text{Pr}_{1.75}\text{Sr}_{0.25}\text{Ni}_{0.75}\text{Co}_{0.25}\text{O}_{4\pm\delta}$ ceramic sample were investigated by means of a Tescan MIRA 3 LMU scanning electron microscope (SEM) with the Oxford Instruments INCA Energy 350 X-ray energy-dispersive microanalysis system (EDX) with an X-max 80 detector and an electron backscatter diffraction system (EBSD) and the INCA Synergy Premium diffraction system with a Nordlys II F+ detector. The electron backscatter diffraction patterns (EBSPs) and EDX maps were collected at HV = 20 kV with the accumulation rate of 170.27 Hz. The cross-section of the ceramic sample was prepared using an Allied MetPrep 4/PH-4 polishing machine system with diamond suspensions. Preliminarily, samples were impregnated with epoxy resin under vacuum to retain the microstructure.

The EDX and EBSD data for the $\text{Pr}_{1.75}\text{Sr}_{0.25}\text{Ni}_{0.75}\text{Co}_{0.25}\text{O}_{4\pm\delta}$ ceramic sample are presented in Fig. 2 and Table 2. EDX analysis confirms that this sample has an impurity phase of

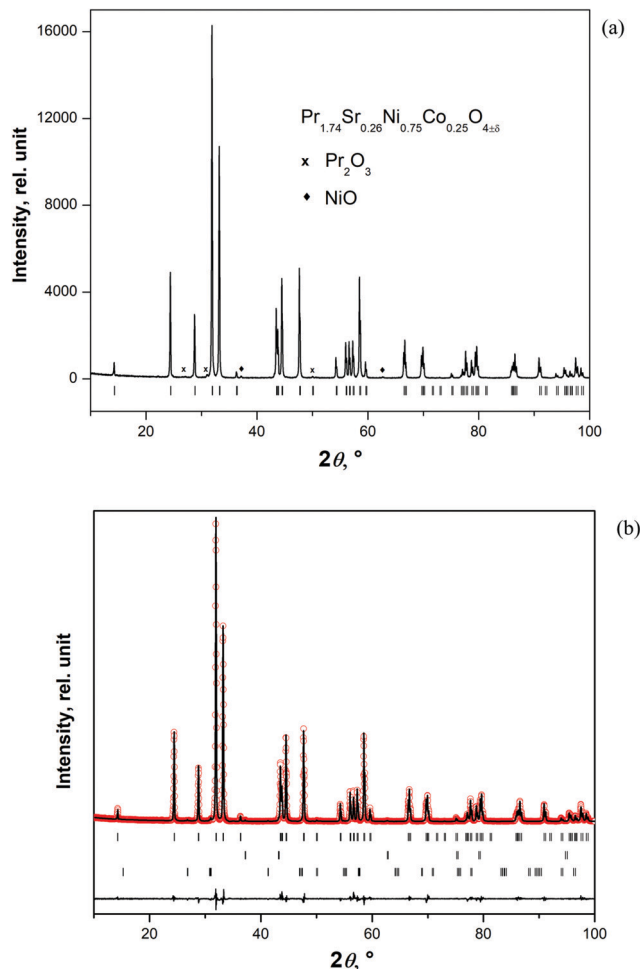


Fig. 1 XRD pattern of $\text{Pr}_{1.75}\text{Sr}_{0.25}\text{Ni}_{0.75}\text{Co}_{0.25}\text{O}_{4\pm\delta}$ (a) and the result of full-profile analysis using the Rietveld method (b).

NiO, as shown in Fig. 2a–f. The studied oxide is found to demonstrate the presence of polycrystalline grains primarily oriented along different crystallographic directions, as shown in Fig. 2i–k. The mean grain diameters of doped praseodymium nickelate oxide are equal to $15 \pm 5 \mu\text{m}$; see Fig. 2i–k. According to EBSD analysis, the crystal structure of the investigated oxide corresponds to the tetragonal K_2NiF_4 -type structure with space group $I4/mmm$. The crystallographic data (crystal lattice parameters $a = 3.82919(5) \text{ \AA}$, $c = 12.3900(2) \text{ \AA}$ and atomic coordinates) were used for EBSD analysis from literature data obtained using the neutron diffraction technique.²³

The XPS study of the cation compositions of the layers near the samples' surfaces was done by means of the X-ray photoelectron spectroscopy Kratos Axis Ultra DLD. The transmission energy is 160 eV (survey) and 40 eV (high resolution spectra). The survey was carried out using AlKa mono with a neutralizer, performing calibration on C 1s –285.0 eV. The dense ceramics for XPS analysis were obtained at two different temperatures: 1200 °C and 1450 °C. These dense ceramics correspond to the samples for the PIE method and the GPE method, respectively. The XPS panoramic spectra of the samples are shown in Fig. 3. The carbon lines on the surface are observed to be due to

Table 1 Cation composition of $\text{Pr}_{1.75}\text{Sr}_{0.25}\text{Ni}_{0.75}\text{Co}_{0.25}\text{O}_{4\pm\delta}$ oxide, at%

Pr	Sr	Ni	Co
1.749 ± 0.010	0.251 ± 0.005	0.747 ± 0.005	0.253 ± 0.005

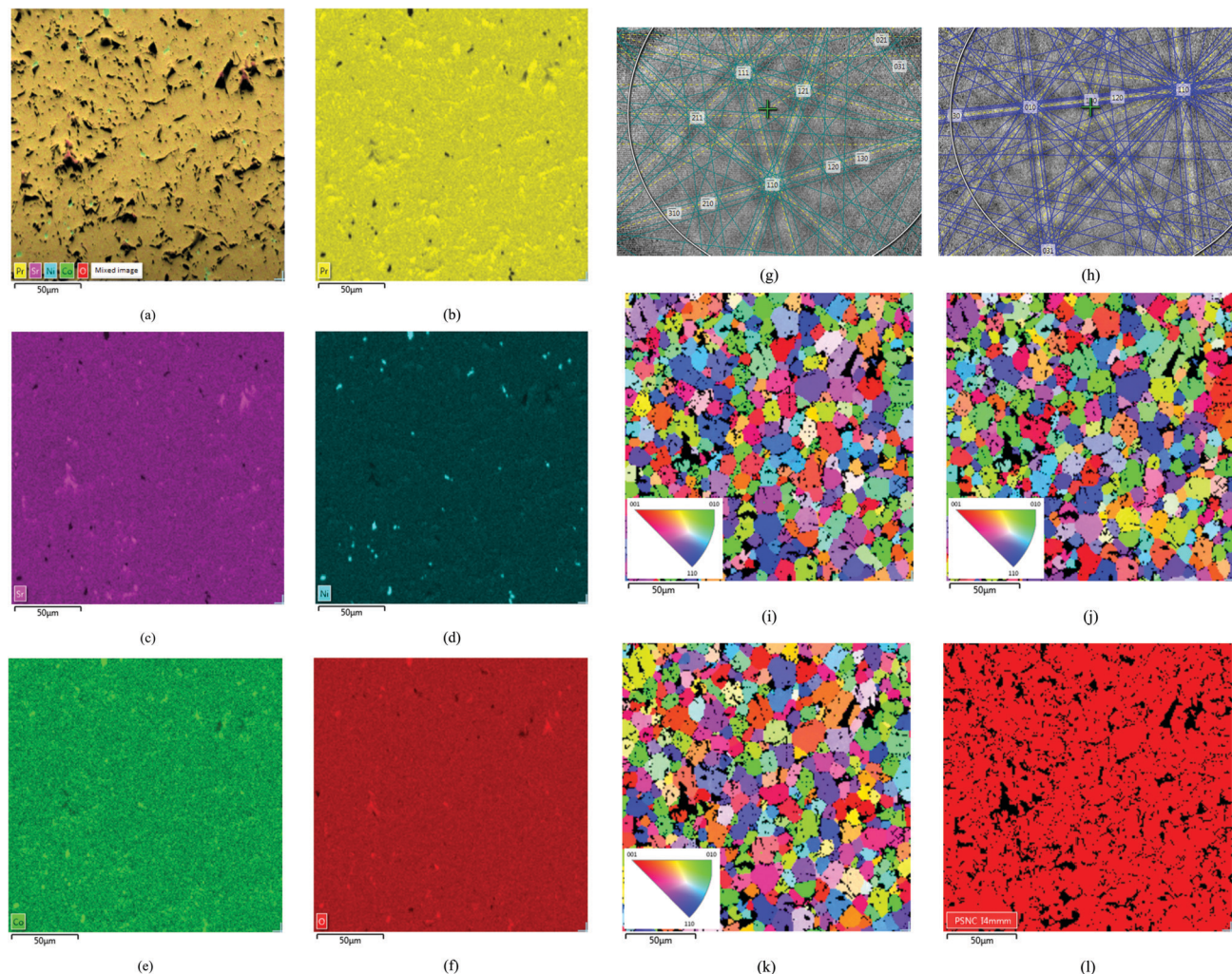


Fig. 2 EDX maps (a – mixed EDX image; b – Pr; c – Sr; d – Ni; e – Co; and f – O), EBSD Kikuchi bands (g – NiO phase and h – main phase), and maps (i – along the OX crystallographic direction; j – along the OY crystallographic direction; k – along the OZ crystallographic direction; and l – EBSD phase map for the main phase) for the $\text{Pr}_{1.75}\text{Sr}_{0.25}\text{Ni}_{0.75}\text{Co}_{0.25}\text{O}_{4\pm\delta}$ sample.

Table 2 EBSD analysis results of the $\text{Pr}_{1.75}\text{Sr}_{0.25}\text{Ni}_{0.75}\text{Co}_{0.25}\text{O}_{4\pm\delta}$ sample

Phase	Phase composition, %	Mean of MAD ^a
$\text{Pr}_{1.75}\text{Sr}_{0.25}\text{Ni}_{0.75}\text{Co}_{0.25}\text{O}_{4\pm\delta}$	84.97	0.53 ± 0.15
Null solutions ^b	15.03	0.00 ± 0.00

^a MAD (Mean Angle Deviation) – the deviation from the theoretical Kikuchi band position. ^b Null solutions correspond to null solutions in the pores of the ceramic sample and to the NiO phase.

surface contamination. The concentrations of the basic elements of $\text{Pr}_{1.75}\text{Sr}_{0.25}\text{Ni}_{0.75}\text{Co}_{0.25}\text{O}_{4\pm\delta}$ on the surface are listed in Table 3. The XPS spectra of 3d and 4d praseodymium lines (Fig. 4) are specific to the trivalent state of the oxide Pr_2O_3 .³⁶ Two states of strontium can be distinguished from the spectra of the Sr 3d-electron line. The spectrum of Sr 3d_{5/2} with the binding energy of 132.5 eV corresponds to strontium carbonate,³⁷ and the binding energy of 134 eV identifies strontium oxide.³⁸ The Ni 2p spectra are typical of divalent nickel, as is identified by the Ni 2p_{3/2} with the binding energy of 855.2 eV.

The kinetics of the oxygen exchange between the gas phase and the powdered oxide was studied using the pulsed isotope exchange method (PIE) in the temperature range of 500–700 °C and the oxygen pressure range of 5.1–40.5 kPa. During the experiment, a powdered sample is loaded in a packed-bed micro-reactor and allowed to equilibrate at a particular oxygen partial pressure and temperature. Maintaining conditions of chemical equilibrium, the response to an ¹⁸O-enriched pulse fed through the reactor under continuous flow conditions is measured by mass spectrometric analysis of the gas phase fractions of oxygen isotopes (¹⁸O₂, ¹⁶O¹⁸O and ¹⁶O₂) at the outline of the reactor.³⁹ The data were processed according to the exponential kinetics model, taking into account only the oxygen exchange stage.

A sintered ceramic sample in slab geometry (9 × 6 × 0.9 mm) was used to determine the oxygen diffusivity in the oxide. The oxygen heterogeneous exchange rate (r_{H}) and the oxygen diffusion coefficient (D) were calculated using the isotope exchange method with gas phase equilibration using a static

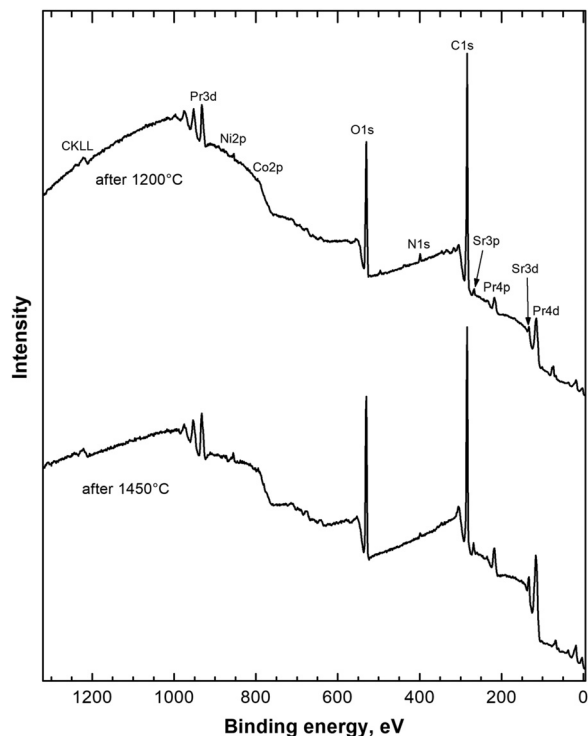


Fig. 3 Panoramic XPS-spectra of the sample after sintering at 1200 °C and 1450 °C.

Table 3 Concentrations of elements on the sample surface (% atom), calculated from the high-resolution XPS spectra

Sample	Pr	Sr	Ni	Co	O
1450 °C (GPE)	20.7	3.7	4.4	5.1	66.1
1200 °C (PIE)	18.6	3.2	2.8	4.0	71.4

circulation experimental rig in the temperature range of 600–850 °C and the oxygen pressure range of 0.9–5.1 kPa. The experimental procedure includes sample pretreatment at $T = 850$ °C and $P_{O_2} = 1$ kPa for 10 hours. After that, the specimen was equilibrated under the particular experimental conditions. The equilibration state is considered to be achieved when the oxygen pressure is constant. After equilibrating, the reactor with the specimen was closed and ^{18}O -oxygen was inlet into the gas contour with the same oxygen pressure as in the reactor. The oxygen isotope exchange began when the reactor was opened. The oxygen isotope composition in the gas phase during the isotope exchange experiment was monitored using an Agilent 5973N quadrupole mass-spectrometer. To prevent gas diffusion limitations, a circulation pump was used.^{40,41}

3. Theory

3.1. Concept of three oxygen exchange types

The concept of three oxygen exchange types was developed in the work of Muzykantov⁴² and Klier.⁴³ They distinguished three

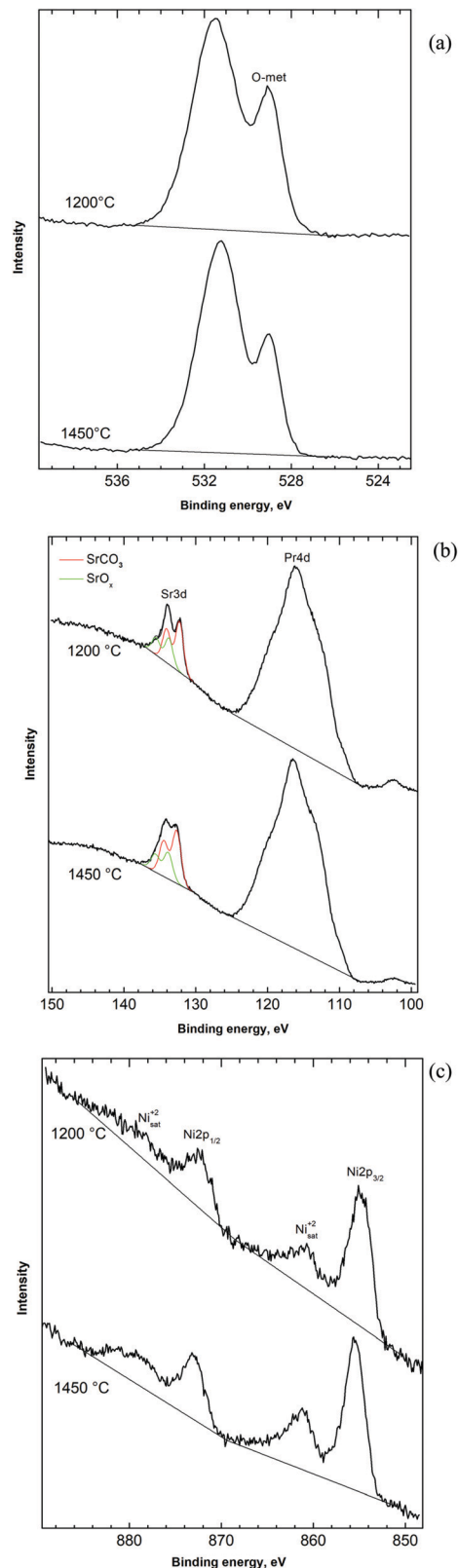
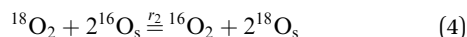
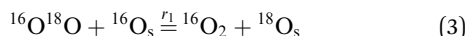


Fig. 4 XPS spectra of high expansion of (a) O 1s, (b) Pr 4d, Sr 3d and (c) Ni 2p.

oxygen exchange types according to the number of surface oxygen atoms participating in one elementary interaction

(0, 1 or 2 oxygen atoms or ions, and ion-radicals) and the corresponding reactions can be written as follows:^{43–45}



where r_0 is the oxygen exchange type (reaction (1)) that represents direct interaction between oxygen atoms in the gas phase without the involvement of oxygen from the solid; r_1 represents the exchange type (reactions (2) and (3)) when one oxygen atom is replaced; and r_2 represents the exchange type when two oxygen atoms are replaced (reaction (4)).

The resulting exchange rate can thus be written as follows:

$$r = r_0 + r_1 + r_2 \quad (5)$$

In previous work,⁴⁴ it was shown that, in order to describe isotope mixing in the “diatomic gas–solid oxide” system, only two equations are necessary and sufficient:

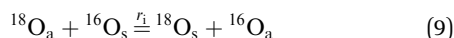
$$\alpha = r_{\text{H}}(\alpha_s - \alpha) \quad (6)$$

$$Z = -rZ + r_2(\alpha_s - \alpha)^2 \quad (7)$$

where α_s and α are the fractions on the surface of the solid oxide and in the gas phase, respectively; r_{H} – the oxygen heterogeneous exchange rate – is the balanced exchange rate under equilibrium conditions normalized by the surface area; and Z is the change in concentration of oxygen molecules of the chosen isotopic composition in comparison with the equilibrium concentration. In (6) and (7) dimensionless rate-values are used for simplicity.

3.2. Two-step model of oxygen exchange and the model with distributed rates

Besides the concept of three oxygen exchange types, recently a two-step model describing the oxygen exchange between the gas phase and the solid oxide was proposed by Den Otter *et al.*⁴⁶ This model includes two sequent stages of oxygen dissociative adsorption (8) and oxygen incorporation (9) with rates r_a and r_i , written here in terms of elementary isotope exchange acts, respectively:



where O_a is the adsorbed oxygen and O_s is the incorporated oxygen.

The oxygen heterogeneous exchange rate can be expressed using r_a and r_i :

$$r_{\text{H}} = \frac{r_a r_i}{r_a + r_i} \quad (10)$$

The rates of the three oxygen exchange types are tied with the oxygen dissociative adsorption rate and oxygen incorporation rate *via* the following equations:

$$r_a = r, \quad (11)$$

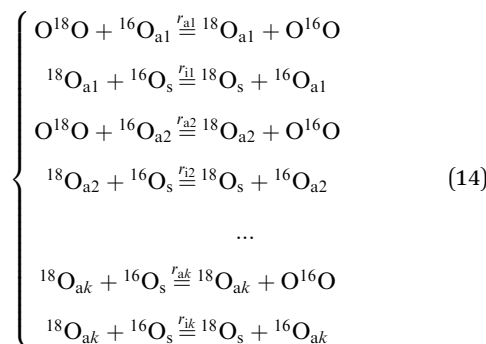
$$r_i = \frac{r_a r_{\text{H}}}{r_a - r_{\text{H}}}. \quad (12)$$

It is essential that the two-step model can be applied to describe the oxygen exchange kinetics only if the following relationship holds:

$$P_{\text{N}} = \frac{2\sqrt{r_0 r_2}}{r_1} = 1 \quad (13)$$

Besides the two-step model, recently a statistical model with distributed oxygen dissociative adsorption and incorporation rates was proposed by Ananyev *et al.*⁹ While the two-step model suggests that all the adsorption centres on the surface of a solid are equal (have equal energy) and the rates can be calculated from eqn (11) and (12) taking into account the ratio $P_{\text{N}} = 1$, the advantage of the statistical model is that it allows the description of the oxygen exchange kinetics and rate calculations in cases when $P_{\text{N}} > 1$.

According to this model, adsorption centres on the surface are not necessarily equal, therefore the dissociative adsorption rate and the incorporation rate have some distribution functions, $f(r_a)$ and $f(r_i)$, respectively. For an ideally homogeneous surface where all adsorption centres are equal, these distribution functions are revealed by δ -functions and the mean values of the dissociative adsorption and incorporation rates correspond to r_a and r_i in the two-step model mentioned above. In turn, in the case of unequal adsorption centres for each k -adsorption centre, we can write two equations, corresponding to the dissociative adsorption and incorporation with the rates r_{ak} and r_{ik} respectively, where k is the number of the adsorption centre.



This parameter P_{N} is associated with oxygen adsorption centre inequality. In the case of distributed r_a and r_i , P_{N} becomes larger than 1.

3.3. Pulse isotopic exchange (PIE) technique and the isotope exchange with gas phase equilibration (IE GPE) method

The PIE method gives only two values of the ^{18}O fraction in the gas phase – before (α_0) and after (α_{τ}) the pulse transmission through the powdered sample, and the oxygen heterogeneous

exchange rate can be calculated according to the following equation:

$$r_H = \ln \frac{\alpha_\tau}{\alpha} \quad (15)$$

It is essential in the PIE method that the values of r and r_2 in the equation system (6) are not calculated independently and are coupled by the following ratio:

$$\frac{rr_2}{r_H^2} = 1 \quad (16)$$

Relationship (16) can be considered to be equivalent to (13), so the oxygen dissociative adsorption and incorporation rates r_a and r_i can only be calculated by employing the PIE method using the two-step model if relation (13) holds between the three oxygen exchange types.

In contrast to the PIE technique, the IE GPE method gives full kinetic information, *i.e.* the ^{18}O fraction time dependence can be obtained for the whole time of exchange between the oxide and the gas phase in the reactor. The isotope exchange experiment finishes when the sample reaches equilibrium or is close to equilibrium. It is worth emphasizing that by treating the experimental data with IE GPE it is possible to calculate the three oxygen exchange type rates independently and thus verify whether relation (13) holds (it is possible to calculate P_N). Therefore, it is also possible to verify the applicability of the two-step model to describe the oxygen exchange kinetics in the particular sample and experimental conditions.

3.4. Oxygen diffusion coefficient calculation

The oxygen diffusion coefficient can be calculated using the model derived by Ezin *et al.*⁴⁷ based on Klier's solution.⁴⁸ The model assumes that (i) exchanging atoms of oxygen are equivalent, *i.e.* the surface of the oxide is homogeneous and (ii) the amount of adsorbed oxygen atoms is negligibly small in comparison with the amount of oxygen atoms or ions on the surface of the oxide. In this model Fick's diffusion eqn (17) and surface exchange equations are solved simultaneously with the boundary and initial conditions (5)–(7):

$$\alpha = D_0 \nabla^2 \alpha \quad (17)$$

4. Results and discussion

Fig. 5a shows typical time dependences of fractions of $^{18}\text{O}_2$, $^{18}\text{O}^{16}\text{O}$, and $^{16}\text{O}_2$ in the gas phase, obtained using the IE GPE method on the $\text{Pr}_{1.75}\text{Sr}_{0.25}\text{Ni}_{0.75}\text{Co}_{0.25}\text{O}_{4\pm\delta}$ ceramics sample. Using the fractions of $^{18}\text{O}_2$, $^{18}\text{O}^{16}\text{O}$, and $^{16}\text{O}_2$, the fraction of oxygen isotope ^{18}O in the gas phase was calculated (see Fig. 5b). The experimental data set was processed using original software⁴⁹ according to the model derived by Ezin *et al.* based on Klier's solution. The processing of the dependence was carried out along two sections of the curve (see the callouts in Fig. 5b); as a result of the processing, the values of r_H , D_1 and D_2 were obtained. The IE GPE data (Fig. 5a) obtained at an oxygen pressure of 1.0 kPa were fitted using two models: the two-step

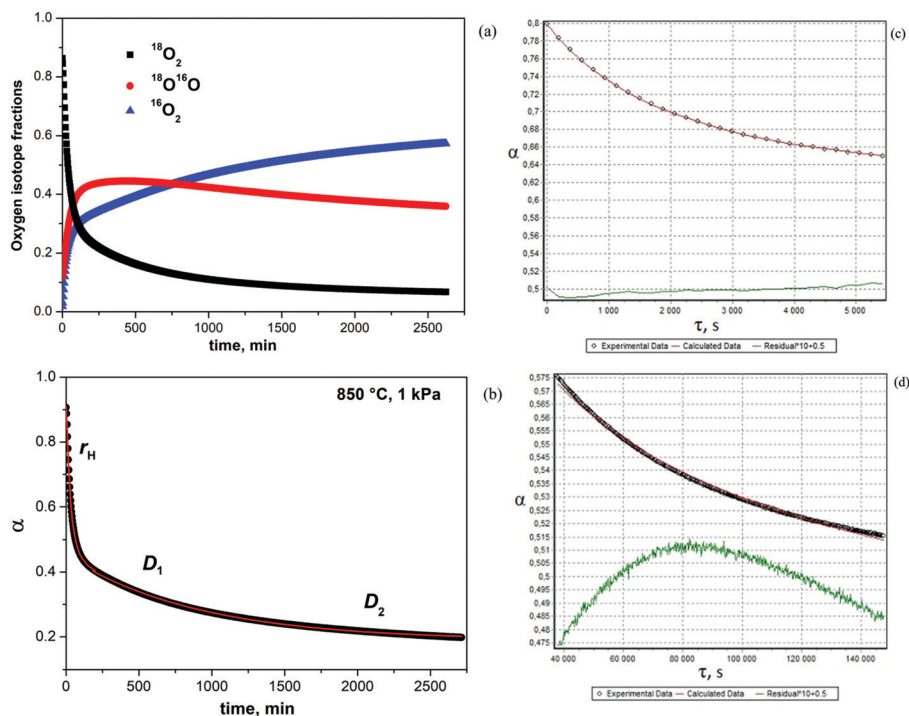


Fig. 5 Typical time dependence of fractions of oxygen isotopes $^{18}\text{O}_2$, $^{18}\text{O}^{16}\text{O}$, and $^{16}\text{O}_2$ in the gas phase at $T = 850\text{ }^\circ\text{C}$ and $P_{\text{O}_2} = 1.0\text{ kPa}$ obtained in the IE GPE experiment (a); time dependence of the fraction of oxygen isotope ^{18}O in the gas phase, obtained in the IE GPE experiment on a dense ceramic sample of $\text{Pr}_{1.75}\text{Sr}_{0.25}\text{Ni}_{0.75}\text{Co}_{0.25}\text{O}_{4\pm\delta}$ and the complete experimental dependence (b); (c) initial area for calculating the oxygen heterogeneous exchange rate (r_H) and the coefficient of "fast" oxygen diffusion (D_1) and (d) second area for calculating the coefficient of "slow" oxygen diffusion (D_2).

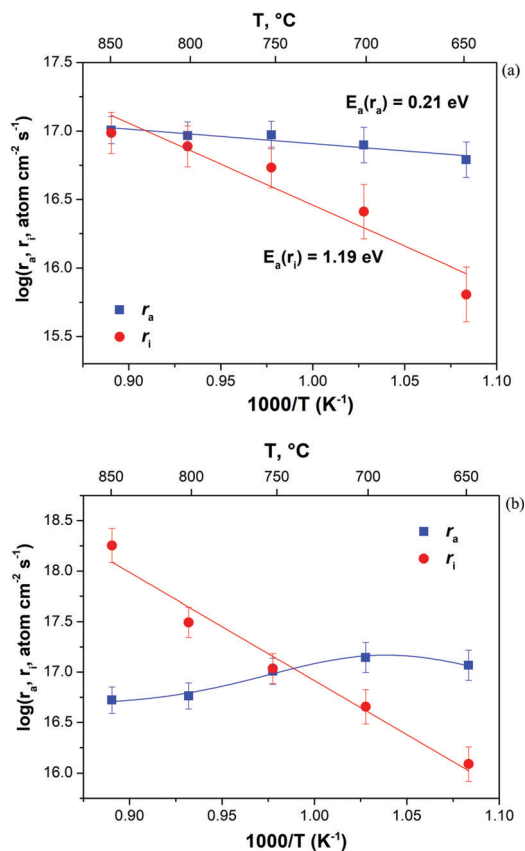


Fig. 6 Temperature dependences of mean values of the oxygen dissociative adsorption and oxygen incorporation rates calculated using the (a) statistical model,⁹ and (b) model by den Otter,⁴⁶ $P_{\text{O}_2} = 1 \text{ kPa}$.

model³⁹ and the statistical model,⁹ and the rates of oxygen dissociative adsorption and oxygen incorporation were calculated. The calculation data are depicted in Fig. 6a (the statistical model) and 6b (the two-step model). The temperature dependence of r_a and r_i obtained using the two-step model is nonlinear and the activation energy for dissociative adsorption is negative. This fact means that the two-step model is inapplicable to describe the oxygen exchange kinetics in the case of the $\text{Pr}_{1.75}\text{Sr}_{0.25}\text{Ni}_{0.75}\text{Co}_{0.25}\text{O}_{4\pm\delta}$ sample in the particular experimental conditions.

Fig. 7 shows the adsorption centre's non-equality P_N parameter values depending on the temperature. Below $750 \text{ }^\circ\text{C}$ the parameter is close to unity and the two-step model can be used. Above $750 \text{ }^\circ\text{C}$ significant deviation of the parameter is observed, which means that only the statistical model can be used for the rate calculations. The r_a and r_i values calculated using the statistical model are the mean values. Calculation of the parameter $\frac{2\sqrt{r_0 r_2}}{r_1}$ thus allows the verification of the applicability of one or the other model in every particular case: for every sample and experimental condition such as temperature and oxygen pressure.

Fig. 8 shows typical temperature dependencies of fractions of $^{18}\text{O}_2$, $^{18}\text{O}^{16}\text{O}$, and $^{16}\text{O}_2$ obtained using the PIE method on the $\text{Pr}_{1.75}\text{Sr}_{0.25}\text{Ni}_{0.75}\text{Co}_{0.25}\text{O}_{4\pm\delta}$ powder. At a temperature of around

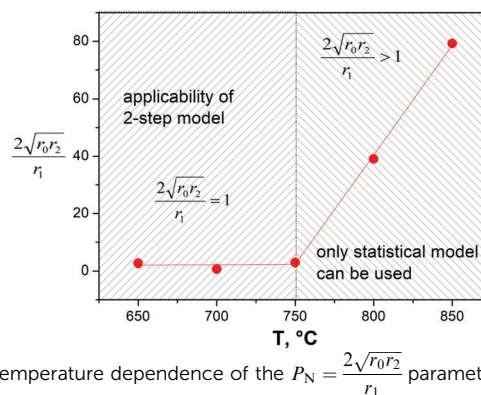


Fig. 7 Temperature dependence of the $P_N = \frac{2\sqrt{r_0 r_2}}{r_1}$ parameter.

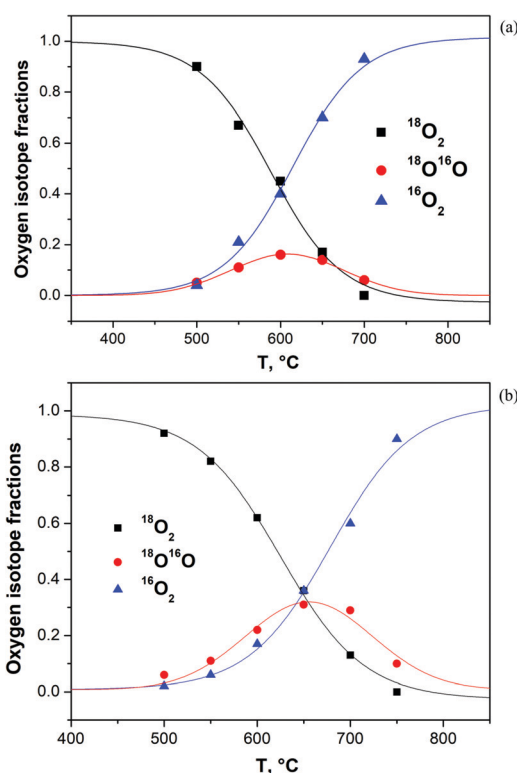


Fig. 8 Temperature dependences of fractions of $^{18}\text{O}_2$, $^{18}\text{O}^{16}\text{O}$, and $^{16}\text{O}_2$ obtained using the PIE method on the $\text{Pr}_{1.75}\text{Sr}_{0.25}\text{Ni}_{0.75}\text{Co}_{0.25}\text{O}_{4\pm\delta}$ powder at (a) $P_{\text{O}_2} = 5.1 \text{ kPa}$ and (b) $P_{\text{O}_2} = 21.3 \text{ kPa}$.

$600 \text{ }^\circ\text{C}$ and $P_{\text{O}_2} = 5.1 \text{ kPa}$, slightly more than half of the original fraction of $^{18}\text{O}_2$ in the pulse volume is converted into $^{18}\text{O}^{16}\text{O}$ and $^{16}\text{O}_2$. The value shifts to higher temperatures with the increase in oxygen pressure. The data were processed according to the exponential kinetics model, taking into account only the oxygen exchange stage.⁴⁶ The rates r_{H} , r_a and r_i calculated from the PIE data using the two-step model are depicted in Fig. 9. One can see the tendency of the rates r_{H} and r_a increasing with increasing P_{O_2} of the experiments (Fig. 9a and b). However, the change in oxygen pressure does not affect the rate of oxygen incorporation (Fig. 9c). The oxygen dissociative adsorption is the rate-determining stage of the exchange process at 5.1 kPa (Fig. 10a). One can conclude that, as the temperature and

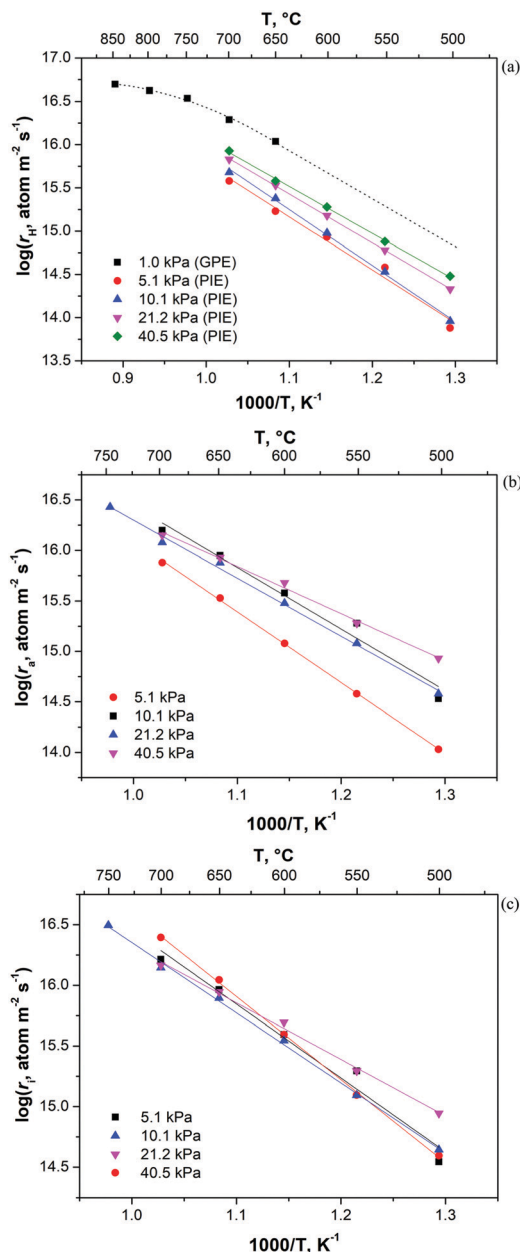


Fig. 9 Temperature dependences of (a) the oxygen heterogeneous exchange rate obtained using PIE and IE GPE methods at different oxygen partial pressure and (b) the oxygen dissociative adsorption rate, and (c) the oxygen incorporation rate at $P_{O_2} = 5.1\text{--}40.5$ kPa obtained using the PIE method on the $Pr_{1.75}Sr_{0.25}Ni_{0.75}Co_{0.25}O_{4+\delta}$ powder.

oxygen pressure increase, the stages of dissociative adsorption and incorporation become competing and the oxygen adsorption apparent activation energy decreases while the oxygen incorporation activation energy changes slightly (Fig. 10b).

Depicted in Fig. 9a is the oxygen heterogeneous exchange rate calculated using both the PIE and IE GPE methods. A good agreement in the activation energies at temperatures below 750 °C is observed between the two methods (Table 4). The apparent activation energy of the oxygen heterogeneous exchange decreases as the temperature increases above 750 °C. Assuming that r_H

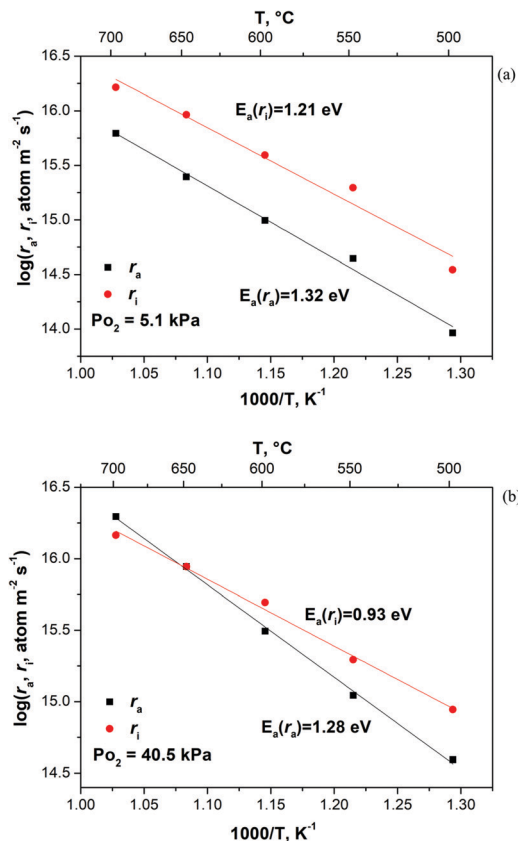


Fig. 10 Temperature dependences of the oxygen adsorption and incorporation rates, obtained using the PIE method at (a) 5.1 kPa and (b) 40.5 kPa.

Table 4 Apparent activation energies, eV

P_{O_2} , kPa	T , °C	r_H	r_a	r_i	D_1	D_2	Method
5.1	500–700	1.24	1.27	1.29	—	—	PIE
10.1		1.37	1.39	1.30	—	—	
40.5		1.13	1.30	0.92	—	—	
21.2	500–750	1.13	1.15	1.11	—	—	
1.0	750–850	0.37	0.21	1.19	0.73	1.06	GPE
	650–750	1.45					

increases with increasing oxygen pressure, it seems surprising that the IE GPE values obtained at lower pressure (1.0 kPa) are higher than the PIE values even for the highest pressure investigated (40.5 kPa). One of the possible reasons is error in the estimation of the ceramic sample surface area. However, we believe that the more probable reason is the difference in the experimental procedures between the two methods: in the IE GPE method, prior to the isotope exchange, the sample undergoes pre-treatment at 850 °C. Therefore, the surface of the sample is degraded. The influence of the grain boundaries in dense ceramics should also be taken into account. Also, the prehistory of the materials differs: in the PIE method the powdered sample was used, which was used after its synthesis at 1200 °C, whereas the GPE method used a dense sample synthesized at a higher temperature (1450 °C). To investigate the surface chemical composition of these materials, XPS research was performed (Fig. 3, 4 and Table 3). A greater content of nickel on the surface is shown

in the case of a sample synthesized at 1450 °C (the GPE method). We believe that its presence on the surface has an effect on the oxygen interphase exchange rate (r_H).

To determine the oxygen diffusivity in $\text{Pr}_{1.75}\text{Sr}_{0.25}\text{Ni}_{0.75}\text{Co}_{0.25}\text{O}_{4\pm\delta}$, a sintered ceramic sample was used. The oxygen heterogeneous exchange rate and oxygen diffusion coefficient (D , $\text{cm}^2 \text{s}^{-1}$) were calculated using the isotope exchange method with gas phase equilibration using a static circulation experimental rig in the temperature range of 600–850 °C and an oxygen pressure range of 1.0–5.1 kPa. The oxygen heterogeneous exchange rate r_H ,

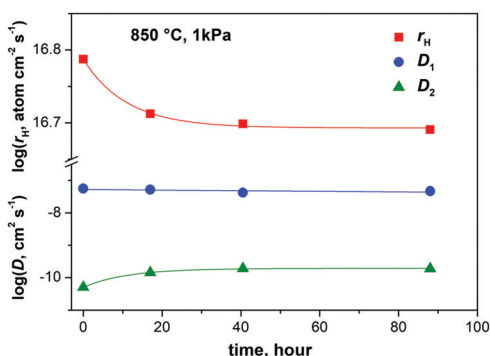


Fig. 11 Time dependences of oxygen heterogeneous exchange rate and two oxygen diffusion coefficients, obtained using the IE GPE method.

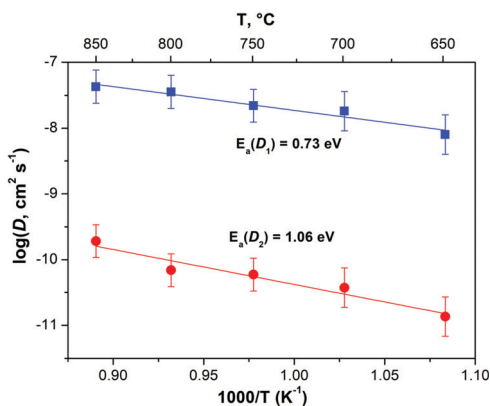


Fig. 12 Temperature dependences of two oxygen diffusion coefficients, obtained using the IE GPE method, $P_{\text{O}_2} = 1$ kPa.

oxygen diffusion coefficient D and the rates of the three oxygen exchange types r_0 , r_1 and r_2 were calculated using the model derived by Ezin *et al.*⁴⁷ based on Klier's solution.⁴⁸

The experiments showed a complicated oxygen isotope exchange kinetic profile including a surface exchange stage as well as at least two diffusion relaxation processes (Fig. 5b). Some of these processes can be registered due to equilibrium not being completely reached in the system. To clarify if the equilibrium affects the oxygen exchange kinetics and try to reveal the physical nature of these processes, measurements were taken during long-term exposures. For this, a freshly prepared sample was loaded into the reactor, heated under the experimental conditions, and was not maintained at equilibrium, and then periodic measurements were performed. The results of the experiment showed that the oxygen heterogeneous exchange rate and the coefficient of “slow” oxygen diffusion (D_2) change with a long exposure and reach a plateau (Fig. 11). The coefficient of “fast” oxygen diffusion (D_1) does not change with time. The apparent activation energy for the two diffusion processes is depicted in Fig. 12.

Since $\text{Pr}_{1.75}\text{Sr}_{0.25}\text{Ni}_{0.75}\text{Co}_{0.25}\text{O}_{4\pm\delta}$ can potentially be used as an electrode material for SOFCs, let us consider obtained values of the oxygen heterogeneous exchange rate and the oxygen diffusion coefficient in comparison with values for similar materials with the Ruddlesden–Popper structure (Table 5). The oxygen diffusion coefficient for $\text{Pr}_{1.75}\text{Sr}_{0.25}\text{Ni}_{0.75}\text{Co}_{0.25}\text{O}_{4\pm\delta}$ is higher compared to other nickelates of lanthanides at 700 °C, and the oxygen heterogeneous exchange rate is close to the undoped nickelates of lanthanides. Based on this comparison one can conclude that $\text{Pr}_{1.75}\text{Sr}_{0.25}\text{Ni}_{0.75}\text{Co}_{0.25}\text{O}_{4\pm\delta}$ is more active than the oxygen reduction reaction for the intermediate temperature range. Doping of lanthanides by strontium or calcium in nickelates leads to an increase in the rate of the oxygen heterogeneous exchange.

The isotopic relaxation method in variance with the temperature-programmed isotopic exchange (TPIE) of oxygen with C^{18}O_2 in the gas phase was used to obtain kinetic values for nickelates of lanthanides.³³ In the processing of the experimental data the assumption of the Arrhenius-type kinetics model was initially laid. However, it could not be correct for $\text{Pr}_2\text{NiO}_{4+\delta}$ according to our results obtained in ref. 35, where we demonstrated that the dependence of the oxygen

Table 5 Values of the oxygen heterogeneous exchange rates and the oxygen diffusion coefficients for materials with the Ruddlesden–Popper structure

Sample	T , °C	P_{O_2} , kPa	E_a , eV		$k_{700^\circ\text{C}}$, cm s^{-1}	$D_{700^\circ\text{C}}$, $\text{cm}^2 \text{s}^{-1}$	Method
			k	D			
$\text{Pr}_{1.75}\text{Sr}_{0.25}\text{Ni}_{0.75}\text{Co}_{0.25}\text{O}_{4\pm\delta}$	650–750	1.0	1.45	0.73	4.4×10^{-7}	1.8×10^{-8}	$^{18}\text{O}_2$
	750–850		0.37				3.8×10^{-11}
$\text{La}_2\text{NiO}_{4+\delta}$ ⁹	600–800	1.33	1.38	1.41	1.8×10^{-7}	1.3×10^{-8}	$^{18}\text{O}_2$
$\text{Pr}_2\text{NiO}_{4+\delta}$ ³⁵	600–700	0.71	2.0	2.0	1.5×10^{-7}	3.2×10^{-9}	$^{18}\text{O}_2$
	700–800		1.4				IE GPE
$\text{Pr}_2\text{NiO}_{4+\delta}$ ³³	N/A	N/A	1.19	0.83	9.5×10^{-5}	7.0×10^{-8}	C^{18}O_2 SSITKA
$\text{Pr}_{1.7}\text{Ca}_{0.3}\text{NiO}_{4+\delta}$ ³³	N/A	N/A	1.35	0.93	2.4×10^{-4}	7.6×10^{-10}	C^{18}O_2 SSITKA
$\text{PrLaNiO}_{4+\delta}$ ⁵⁰	500–700	21	1.88	0.67	1.5×10^{-5}	6.0×10^{-8}	$^{18}\text{O}_2$ SIMS

heterogeneous exchange rate had no Arrhenius-type behavior. Moreover, the authors in ref. 33 suggested the presence of an additional slow diffusion channel, observed as a separate peak on the TPIE curve. The authors asserted that the fast diffusion channel corresponds to the cooperative mechanism, and the slow diffusion channel is related to oxygen migration in the perovskite layers and complicated transport of the interstitial oxygen atoms in the near-dopant positions. However, we suppose that it is impossible to unambiguously identify the path of the fast and slow oxygen diffusion reaction. We can offer several explanations for the two observed oxygen diffusion coefficients: (1) different oxygen diffusivities in the bulk and along the grain boundaries; (2) the presence of different defect types (vacancies and interstitials); (3) the presence of inhomogeneity in $\text{Pr}_{1.75}\text{Sr}_{0.25}\text{Ni}_{0.75}\text{Co}_{0.25}\text{O}_{4\pm\delta}$ with differently oriented grains in polycrystalline specimens along “fast” and “slow” diffusion pathways in the Ruddlesden–Popper structure; and (4) substantial anisotropy of the oxygen atoms due to strontium in the crystal structure.²³

5. Conclusions

The present work focuses on the investigation of the oxygen surface exchange kinetics and diffusion in $\text{Pr}_{1.75}\text{Sr}_{0.25}\text{Ni}_{0.75}\text{Co}_{0.25}\text{O}_{4\pm\delta}$ by means of two different methods: pulsed isotope exchange and isotope exchange with gas phase equilibration.

The oxygen heterogeneous exchange rate r_{H} , oxygen dissociative adsorption rate r_{a} and oxygen incorporation rate r_{i} were calculated using the pulsed isotope exchange method in the temperature range of 500–750 °C and the oxygen pressure range of 5.1–40.5 kPa. With increase in the oxygen pressure, r_{a} and r_{H} also increase, while r_{i} changes slightly. In the temperature range of 650–750 °C oxygen dissociative adsorption is the rate-determining stage; however, with increasing temperature the rates become competing.

The oxygen heterogeneous exchange rate and the oxygen diffusion coefficient were calculated using the isotope exchange with gas phase equilibration method in the temperature range of 600–850 °C and the oxygen pressure range of 1.0–5.1 kPa. The experiments showed a complicated oxygen isotope exchange kinetic profile, including a surface exchange stage as well as at least two diffusion relaxation processes. We suppose that these two diffusion processes can be associated either with the presence of different defect types (oxygen interstitials and vacancies) or with different oxygen diffusivities in the bulk and along the grain boundaries. These two relaxation processes can also be associated with the observed presence of two phases of $\text{Pr}_{1.75}\text{Sr}_{0.25}\text{Ni}_{0.75}\text{Co}_{0.25}\text{O}_{4\pm\delta}$ with different oxygen content and therefore different oxygen diffusivity.

Calculation of the rates r_{a} and r_{i} using the two models showed that the two-step model is only applicable at temperatures below 750 °C for the description of the oxygen exchange with $\text{Pr}_{1.75}\text{Sr}_{0.25}\text{Ni}_{0.75}\text{Co}_{0.25}\text{O}_{4\pm\delta}$. Above 750 °C, only the statistical model can be used to describe the oxygen exchange kinetics. Verification of the applicability of the two-step model was carried

out for the $\text{Pr}_{1.75}\text{Sr}_{0.25}\text{Ni}_{0.75}\text{Co}_{0.25}\text{O}_{4\pm\delta}$ sample under particular experimental conditions.

Conflicts of interest

There are no conflicts to declare.

Acknowledgements

The work was done using Unique scientific setup “Isotopic exchange” of the shared access center “Composition of Compounds” of IHTe UB RAS. The isotope exchange study is supported by the President Grant MД-6758.2018.3. The educational activities of Ph.D. involved into this work are supported by the Act 211 of the Government of the Russian Federation, Agreement No. 02.A03.21.0006.

References

- 1 E. S. Raj, K. F. E. Pratt, S. J. Skinner, I. P. Parkin and J. A. Kilner, *Chem. Mater.*, 2006, **18**, 3351.
- 2 T. Ogier, F. Chauveau, J.-M. Bassat, F. Mauvy, J.-C. Grenier, J. Mougín and M. Petitjean, *ECS Trans.*, 2011, **35**, 1817.
- 3 K. C. Wincewicz and J. S. Cooper, *J. Power Sources*, 2005, **140**, 280.
- 4 A. I. Popov and E. Balanzat, *Nucl. Instrum. Methods Phys. Res., Sect. B*, 2000, **166**, 305.
- 5 FUEL CELLS, *Problems and Solutions*, John Wiley & Sons, 2nd edn, 2012, p. 385.
- 6 X. Zhu and W. Yang, *Mixed Conducting Ceramic Membranes: Fundamentals, Materials and Applications*, Springer-Verlag GmbH Germany, 2017, p. 367.
- 7 H. Klym, A. Ingram, O. Shpotyuk, I. Hadzaman, V. Solntsev, O. Hotra and A. Popov, *Low Temp. Phys.*, 2016, **42**(7), 764.
- 8 S. N. Ruddlesden and P. Popper, *Acta Crystallogr.*, 1957, **10**(7), 538.
- 9 M. V. Ananyev, E. S. Tropin, V. A. Eremin, A. S. Farlenkov, A. S. Smirnov, A. A. Kolchugin, N. M. Porotnikova, A. V. Khodimchuk, A. V. Berenov and E. K. Kurumchin, *Phys. Chem. Chem. Phys.*, 2016, **18**, 9102.
- 10 F. M. Sapountzi, J. M. Gracia, C.-J. Weststrate, H. O. A. Fredriksson and J. W. Niemantsverdriet, *Prog. Energy Combust. Sci.*, 2017, **58**, 1.
- 11 J. T. S. Irvine, D. Neagu, M. C. Verbraeken, C. Chatzichristodoulou, C. Graves and M. B. Mogensen, *Nat. Energy*, 2016, **1**, 1.
- 12 E. Dogdibegovic, Q. Cai, N. S. Alabri, W. Guan and X.-D. Zhou, *J. Electrochem. Soc.*, 2017, **164**(2), F99.
- 13 J. M. Bassat, P. Odier, A. Villesuzanne, C. Marin and M. Pouchard, *Solid State Ionics*, 2004, **167**, 341.
- 14 J. Dailly, S. Fourcade, A. Largeteau, F. Mauvy, J. C. Grenier and M. Marrony, *Electrochim. Acta*, 2010, **55**, 5847.
- 15 C. Ferchaud, J. C. Grenier, Y. Z. Steenwinkel and M. M. A. Tuel, *J. Power Sources*, 2011, **196**, 1872.
- 16 M. A. Laguna-Bercero, H. Monzón, A. Larrea and V. M. Orera, *J. Mater. Chem. A*, 2016, **4**, 1446.

- 17 A. V. Kovalevsky, V. V. Kharton, A. A. Yaremchenko, Y. V. Pivak, E. V. Tsipis, S. O. Yakovlev, A. A. Markov, E. N. Naumovich and J. R. Frade, *J. Electroceram.*, 2007, **18**, 205.
- 18 T. Broux, C. Prestipino, M. Bahout, S. Paofai, E. Elkaïm, V. Vibhu, J.-C. Grenier, A. Rougier, J.-M. Bassat and O. Hernandez, *Dalton Trans.*, 2016, **45**, 3024.
- 19 S. S. Bhoga, A. P. Khandale and B. S. Pahune, *Solid State Ionics*, 2014, **262**, 340.
- 20 C. Allançon, P. Odier, J. M. Bassat and J. P. Loup, *J. Solid State Chem.*, 1997, **131**, 167.
- 21 Y. Takeda, R. Kanno, M. Sakano, O. Yamamoto, M. Takano, Y. Bando, H. Akinaga, K. Takita and J. B. Goodenough, *Mater. Res. Bull.*, 1990, **25**, 293.
- 22 M. J. Sayagues, M. Vallet-Regi, A. Caneiro and J. M. Gonzalez-Calbet, *Solid State Ionics*, 1993, **66**, 21.
- 23 S. Ya. Istomin, O. M. Karakulina, M. G. Rozova, S. M. Kazakov, A. A. Gippius, E. V. Antipov, I. A. Bobrikov, A. M. Balagurov, A. A. Tsirlin, A. Michau, J. J. Biendicho and G. Svensson, *RSC Adv.*, 2016, **6**, 33951.
- 24 H. Dulli, P. A. Dowben, S. H. Liou and E. W. Plummer, *Phys. Rev. B: Condens. Matter Mater. Phys.*, 2000, **62**(22), R14629.
- 25 J. Druce, H. Tellez, M. Burriel, M. D. Sharp, L. J. Fawcett, S. N. Cook, D. S. McPhail, T. Ishihara, H. H. Brongersma and J. A. Kilner, *Energy Environ. Sci.*, 2014, **7**(11), 3593.
- 26 W. Lee, J. W. Han, Y. Chen, Z. Cai and B. Yildiz, *J. Am. Chem. Soc.*, 2013, **135**(21), 7909.
- 27 E. Boehm, J.-M. Bassat, P. Dordor, F. Mauvy, J.-C. Grenier and Ph. Stevens, *Solid State Ionics*, 2005, **176**, 2717.
- 28 S. J. Skinner and J. A. Kilner, *Solid State Ionics*, 2000, **135**, 709.
- 29 H. Zhao, F. Mauvy, C. Lalanne, J.-M. Bassat, S. Fourcade and J.-C. Grenier, *Solid State Ionics*, 2008, **86–88**, 2000.
- 30 N. Gauquelin, *PhD thesis*, University of Rennes, France and RWTH Aachen, Germany, 2010.
- 31 M. Burriel, G. Garcia, J. Santiso, J. A. Kilner, R. J. Chater and S. J. Skinner, *J. Mater. Chem.*, 2008, **18**, 416.
- 32 J. A. Kilner and C. K. M. Shaw, *Solid State Ionics*, 2002, **154–155**, 523.
- 33 E. Y. Pikalova, A. A. Kolchugin, V. A. Sadykov, E. M. Sadovskaya, E. A. Filonova, N. F. Ereemeev and N. M. Bogdanovich, *Int. J. Hydrogen Energy*, 2018, **43**(36), 17373.
- 34 E. S. Tropin, M. V. Ananyev, A. S. Farlenkov, A. V. Khodimchuk, A. V. Berenov, A. V. Fetisov, V. A. Eremin and A. A. Kolchugin, *J. Solid State Chem.*, 2018, **262**, 199.
- 35 N. M. Porotnikova, A. V. Khodimchuk, M. V. Ananyev, V. A. Eremin, E. S. Tropin, A. S. Farlenkov, E. Yu. Pikalova and A. V. Fetisov, *J. Solid State Electrochem.*, 2018, **22**, 2115.
- 36 H. Ogasawara, A. Kotani, R. Potze, G. A. Sawatzky and B. T. Thole, *Phys. Rev. B: Condens. Matter Mater. Phys.*, 1991, **44**(11), 5465.
- 37 J. F. Moulder, W. F. Stickle, P. E. Sobol and K. D. Bomben, *Handbook of X-ray Photoelectron Spectroscopy*, ULVAC-PHI, Inc., Chigasaki, 1995, p. 261.
- 38 H. Van Doveren and J. A. T. H. Verhoeven, *J. Electron Spectrosc. Relat. Phenom.*, 1980, **21**(3), 265.
- 39 H. J. M. Bouwmeester, Ch. Song, J. Zhu, J. Yi, M. van Sint Annaland and B. A. Boukamp, *Phys. Chem. Chem. Phys.*, 2009, **11**, 9640.
- 40 M. V. Ananyev and E. K. Kurumchin, *Russ. J. Phys. Chem.*, 2010, **84**(6), 1039.
- 41 M. V. Ananyev, E. K. Kurumchin and N. M. Porotnikova, *Russ. J. Electrochem.*, 2010, **46**, 789.
- 42 V. S. Muzykantov, *Kinet. Catal.*, 1965, **6**, 952.
- 43 K. Klier, J. Novakova and P. Jiru, *J. Catal.*, 1963, **2**(6), 479.
- 44 G. K. Borekov and L. A. Kasatkina, *Russ. Chem. Rev.*, 1968, **37**(8), 613.
- 45 V. S. Muzykantov, G. I. Panov and G. K. Borekov, *Kinet. Catal.*, 1973, **14**, 948.
- 46 M. W. Den Otter, B. A. Boukamp and H. J. M. Bouwmeester, *Solid State Ionics*, 2001, **139**, 89.
- 47 A. N. Ezin, V. I. Tsidilkovski and E. K. Kurumchin, *Solid State Ionics*, 1996, **84**, 105.
- 48 K. Klier and E. Kucera, *J. Phys. Chem. Solids*, 1966, **27**, 1087.
- 49 State Registration Certificate of Computer Program no. 2011614003, Russia, 2011.
- 50 V. Vibhu, A. Rougier, C. Nicolle, A. Flura, J.-C. Grenier and J.-M. Bassat, *Solid State Ionics*, 2015, **278**, 32.